ADVANCED ENERGY MATERIALS
www.advenergymat.de

Nonuniform Ionic and Electronic Transport of Ceramic and Polymer/Ceramic Hybrid Electrolyte by Nanometer-Scale Operando Imaging for Solid-State Battery

Chun-Sheng Jiang, Nathan Dunlap, Yejing Li, Harvey Guthrey, Ping Liu, Se-Hee Lee, and Mowafak M. Al-Jassim*

Replacing the liquid electrolyte in lithium batteries with solid-state ion conductor is promising for next-generation energy storage that is safe and has high energy density. Here, nanometer-resolution ionic and electronic transport imaging of Li_3PS_4 (LPS), a solid-state electrolyte (SSE), is reported. This nm resolution is achieved by using a logarithm-scale current amplifier that enhances the current sensitivity to the fA range. Large fluctuations of ion current—one to two orders of magnitude on the LPS and on the LPS region of a polymer/LPS bulk hybrid SSE—that must be mitigated to eliminate Li dendrite formation and growth, are found. This ion current fluctuation is understood in terms of highly anisotropic transport kinetic barriers along the different crystalline axes due to different grain orientations in the polycrystalline and glass ceramic materials. The results on the bulk hybrid SSE show a sharp transition of ionic and electronic transport at the LPS/polymer boundary and decreases in average ionic current with decreasing polyimine particle size and with extensive cycling. The results elucidate the mechanism of polyimine extension into interparticles to prevent Li dendrite growth. This work opens up novel characterization of charge transport, which relates to Li plating and stripping for solid-state-batteries.

1. Introduction

Solid-state electrolytes (SSEs) are among the most promising electronic separators and ionic conductors to enable high-energy-density Li metal batteries, and they can greatly improve safety by replacing the traditional flammable liquid electrolyte.[1–4] In recent years, the ion conductivity of SSEs has been greatly enhanced to a level comparable to that of liquid electrolytes,[2,5–7] which is critical for fast charging/discharging. To date, ion transport has primarily been characterized by macroscopic measurements such as electrochemical impedance spectroscopy (EIS), galvanostatic profiles of charging/discharging, and nuclear magnetic resonance relaxometry.[8,9] These measurements essentially reflect an average of microscopic ion-transport phenomena. Ion transport in SSEs can be far more complicated than in liquid electrolytes, where it is fundamentally isotropic and uniform. Furthermore, detailed microscopic transport characterization studies are currently lacking in this field.[10] Theoretical studies have proposed that ion transport can be governed by highly crystalline-orientation-dependent ionic hopping inside the ceramic lattice,[11,12] and some SSEs can even act as 1D[13–15] or 2D ion conductors.[16] The polycrystalline and glassy ceramic ion conductors often contain multiple phases with different crystalline structures and significant chemical nonuniformity; these phases thus complicate efforts to define ion-transport properties. The bulk SSE may also have a significant volume fraction of disordered grain/particle boundaries versus interior regions of small-sized grains.[17,18] All these factors can complicate our understanding of ion-transport phenomena. In addition, ion transport can be further complicated by the formation of the solid-electrolyte interphase (SEI) layer through chemical reaction of the SSE and electrode materials[19,20] and by the formation of the space-charge layer by Li-ion transfer across the interfaces.[21,22] To expose the details of ion-conduction processes, it is necessary to use characterization methods that measure ion transport with nm-scale spatial resolution to improve our understanding and tune the ion conduction in solid-state batteries (SSBs).

Currently, the two major directions—inorganic ceramic-based and polymer-based—for developing SSEs pose challenges unique to the chosen approach. Inorganic ceramics SSEs have superior ion conductivity, comparable to liquid electrolyte, but they are also accompanied by chemical interaction

Dr. C.-S. Jiang, Dr. H. Guthrey, Dr. M. M. Al-Jassim
National Renewable Energy Laboratory
Golden, CO 80401, USA
E-mail: chun.sheng.jiang@nrel.gov
Dr. N. Dunlap, Prof. S.-H. Lee
Department of Mechanical Engineering
University of Colorado
Boulder, CO 80309, USA
Dr. Y. Li, Prof. P. Liu
Department of NanoEngineering
University of California San Diego
La Jolla, CA 92093, USA
The ORCID identification number(s) for the author(s) of this article can be found under https://doi.org/10.1002/aenm.202000219.

DOI: 10.1002/aenm.202000219

with the Li anode and cathode, which leads to instability at the SSE/Li interface.[23–27] On the other hand, polymer electrolytes show good stability and plasticity at the Li interface, but they have poor ion conductivity.[28] One promising approach is to use a ceramic and polymer hybrid, and many efforts focus on engineering the SSE/Li interface or modifying the SSE bulk of such hybrid materials.[29–33] In addition to the issue of interface stability, another challenge in developing SSBs is Li dendrite formation and growth. Dendrite growth has been observed in all the major ceramic SSEs developed so far, making it a global concern for these materials.[34–36] Li dendrites cause SSB shunting and failure and must be eliminated before SSEs can be used in commercial SSB products. The Li dendrite can start from either the SSE/electrode interface or from inside the SSE bulk.[36–39] The origin can be a chemical or crystalline defect, or, based on the present work, it may simply be from transport nonuniformities. In any case, the formation and growth of dendrites originates directly from nonequilibrium or uneven ion transport, accompanied by an electronic transport to balance the charge or reduce Li ion. Therefore, to further develop SSBs, it is critical to understand both the ionic and electronic transport in nonuniform SSE material as well as the SSE/electrode interface.

In this contribution, we report on developing an ionic and electronic transport imaging technique based on atomic force microscopy (AFM) to investigate the nm-scale inhomogeneity of ionic and electronic transport. A major imaging challenge is the small current—less than a picoampere (pA)—resulting from the small probe size required for nm-scale spatial resolution. We used a logarithm-scale amplifier to enhance the current sensitivity to the femtoampere (fA) range, as opposed to conventional amplifiers that operate in the nanoampere (nA) or sub-nA range. We found that ionic transport across the SSE is highly nonuniform, fluctuating by more than one order of magnitude. The electronic current is many orders of magnitude smaller than the ion current, consistent with a working electronic separator and ion conductor. Furthermore, we found that the ion transport in the polymer/ceramic bulk hybrid SSE[29,30] proceeds through the ceramic and is blocked by polymer particles, with a sharp transition at the polymer/LPS boundary. Additionally, we found that the ion conductivity decreases with both decreasing polymer particle size and increasing charging/discharging cycling. These results agree with the self-healing model previously proposed, where the polymer forms an optimized matrix between the ceramic particles through the cycling process.[29,30]

2. Results

Based on the contact mode of AFM, we set up a half battery cell consisting of AFM probe, SSE, and Li metal (**Figure 1**) to image the ionic and electronic transport at the nm-scale. A bias voltage (*Vs*) is applied to the Li metal side, and the probe is virtually grounded—which means that the probe potential is maintained at the ground level but does not connect to the ground—to measure the current through the probe. With a negative *Vs*, the electronic leakage current (I_e) is measured, but no Li ionic current (I_i) flows in this polarity (see Figure 1) because there is no Li at the probe side that can supply Li flowing through the SSE. At the same time, it is impossible under a small *Vs* (<0.5 V) to generate ion current by extracting Li ion in the SSE to the Li/SSE interface and further reducing it to Li atom by flowing electrons through the circuit.[11–13,40] With a positive *Vs*, both the

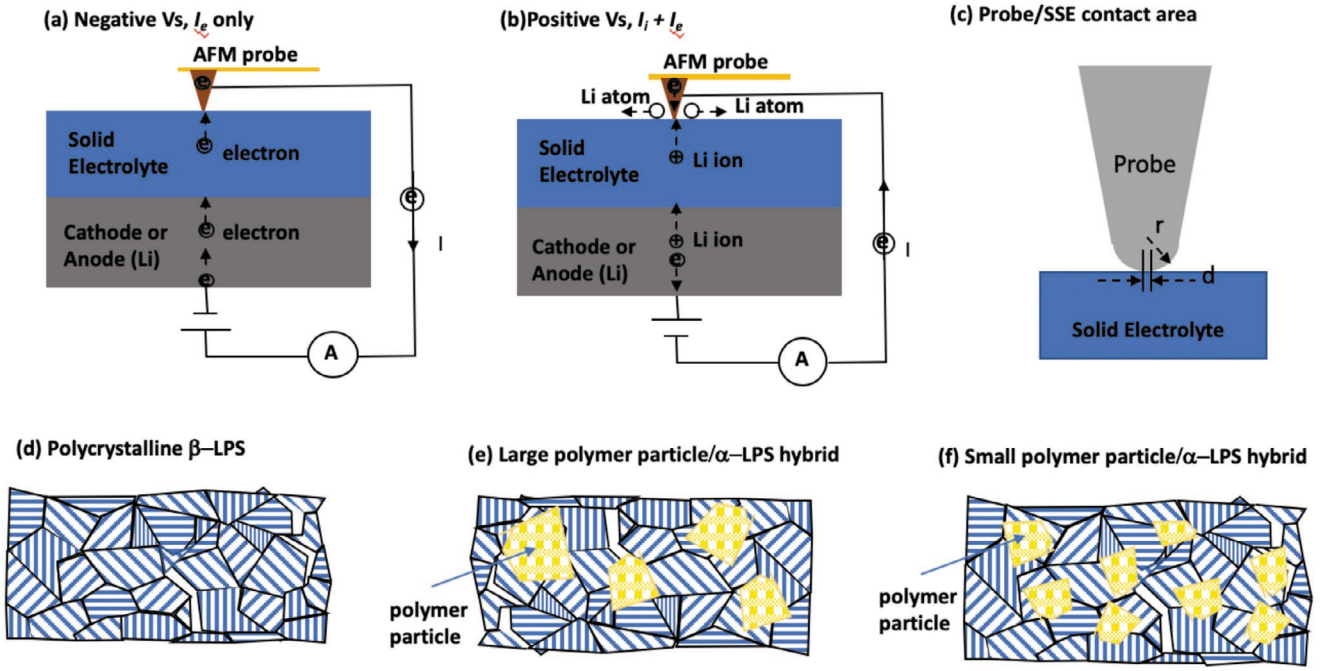

Figure 1. Schematics of the transport imaging setup illustrating a) electronic transport, b) ionic and electronic transport, and c) probe/SSE contact area, *Vs* = bias voltage, I_e = leakage current, I_i = ionic current. Figure 1d–f shows schematics of sample structures involved in this paper: d) polycrystalline β-LPS, e) hybrid SSE of α-LPS with large polymer particles, f) hybrid SSE with small polymer particles. The sizes of polycrystalline LPS and polymer particles are not in scales.

ionic conduction and electronic leak current ($I_e + I_i$) can flow (Figure 1b). Because the electronic current should be about symmetrical with the *Vs* polarity—from the current difference under positive and negative polarities—the ionic current can be deduced. The ionic current is usually several orders of magnitude larger than the electronic current for an SSE, and ion current fully dominates the measured current with a positive *Vs*. We will first show the ionic and electronic imaging results on the polycrystalline ceramic Li_3PS_4 (LPS) SSE, then discuss the results on a polyimine/LPS bulk hybrid SSE.

2.1. Ionic and Electronic Transport Imaging on LPS Solid Electrolyte

Figure 2 shows ion-current images taken on the LPS in a half cell at the same sample area and with different *Vs* values. The ion current is highly nonuniform, with an overall fluctuation of typically one to two orders of magnitude (Figure 2c,e). The sizes of large current fluctuations are several μm; however, the current also fluctuates in smaller amplitudes and in smaller sizes of 1 to several 100 nm. The scale bar in the current images is a logarithmic scale, with the average value indicated in the middle of the bar; the dark and bright represents larger and smaller currents, respectively. The fluctuation of ion current appears to be randomly distributed, and the current distribution changes significantly with *Vs*. The overall current value in this sample area did not change significantly with increasing *Vs* from 0.1 to 0.25 V; however, we observed increases in other areas. This difference may depend on the local chemical fluctuation and grain structures such as crystalline orientation and defect configurations, which will be discussed in the Discussions section. There are partial topographic effects on the current images in some local areas such as the one indicated by the dashed ovals, which is identified by the correlation in the same sample location between the AFM and different current images. However, in comparing the current and topographic images, the overall current does not strictly follow the topography; thus, the current images are not dominated by the surface morphology.

The average ion current is on the order of pA, and the current density is 1 pA per 100 nm^2 = 10 mA cm^{-2} or less, assuming that the probe/SSE contact area is comparable to the probe radius (100 nm) or less because the mild probe/sample contact force would not press the probe deeply into the sample. This current density is comparable to the normal charging rate of a battery, and we did not observe any SSE damage that would cause changes in the appearance of the surface morphology. The probe/SSE contact force is on the order of nanonewtons (nN), and the *Vs* that we applied from the sample side is <0.5 V; under these mild experimental conditions, no changes were observed in the SSE over time. This setup is a two-terminal resistance measurement: the measured overall resistance is dominated by the resistance of the local nm volume of the sample directly beneath the probe, and the current is determined by this local resistance. Contributions of resistance from other parts of the SSE decrease rapidly with distance away from the local area because the ion-current routes increase

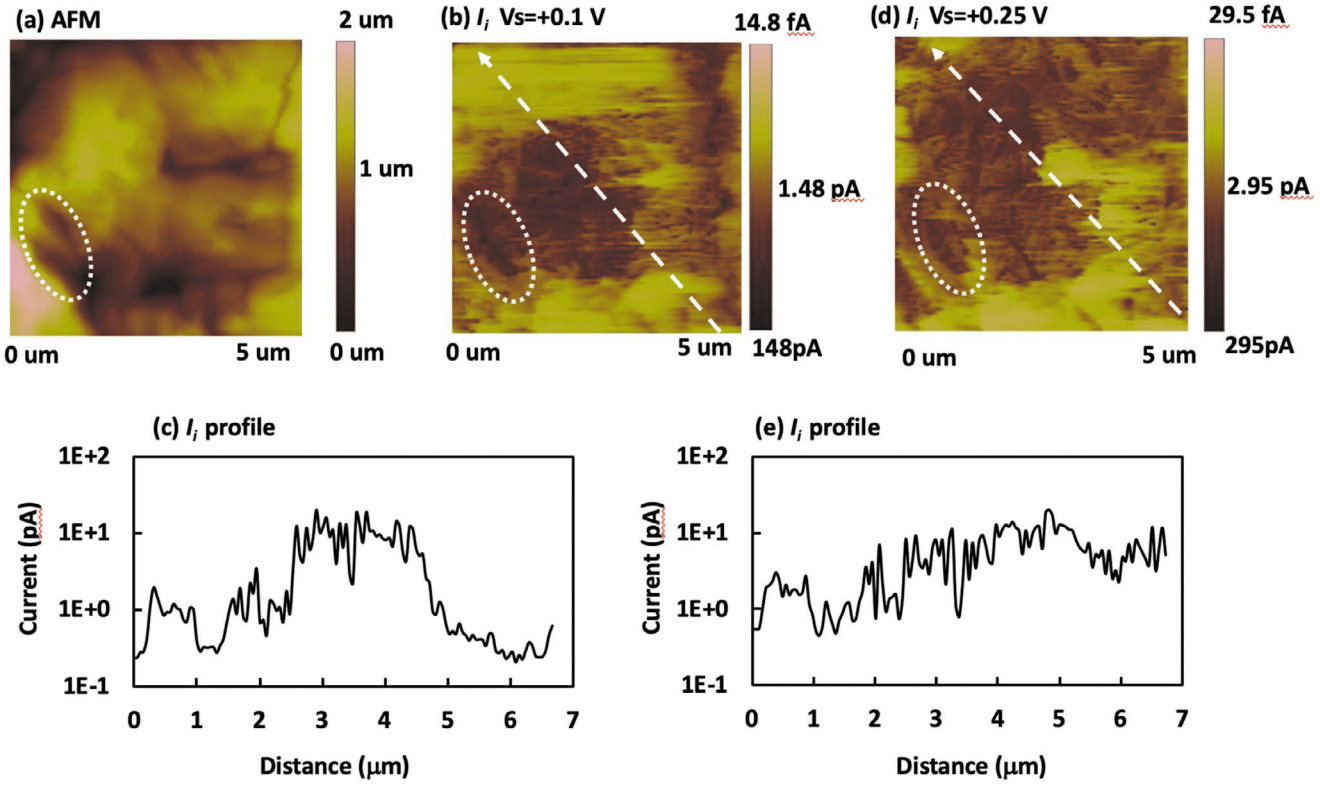

Figure 2. a) An AFM image and (b) and (d) show ion-current images taken on the same area of the LPS SSE with positive *Vs* = +0.1 V and 0.25 V, respectively. (c) and (e) show current line profiles along the dashed lines in (b) and (d), respectively.

rapidly.[41–43] Therefore, the current image is determined mainly by the local ion conductivity of the SSE in the near-surface region, and the image has spatial resolutions in the nm scale, which is comparable to the probe/SSE contact area.

In fact, the measured current under a positive *Vs* is the sum of ion current and electronic current (Figure 1b). Under a negative *Vs*, the measured current is only electronic current, and in all the working SSE that we measured, the electronic current is several orders of magnitude smaller than ion current. Therefore, the current images with a positive *Vs* are dominated by ion current. The electronic current is about five orders of magnitude smaller than the ion current in the same area and with similar voltage amplitude but having opposite polarity (**Figure 3**). The current is not an ionic current flowing from either the probe or surface side to the Li/SSE interface due to pre-plating of Li with a positive *Vs*, as we confirmed that the electronic current amplitude with a negative *Vs* does not vary depending on whether or not the scanned area was pre-plated with positive *Vs*. In fact, we never observed a topography change by the Li plating with a positive *Vs*, probably because Li atoms plated by the AFM probe are mobile and were pushed out of the scanned area by the probe being in scanning mode. The mobility of Li atoms on a surface should be higher than Li atoms at the Li/SSE interface, where the plated atoms should be anchored by bonding energy at the interface.

The leakage electronic current is approaching the detection limit of the amplifier, and the absolute value is not accurate considering the narrow bandwidth at the small current values. However, the approximate orders of magnitude are confirmed. The electronic current also fluctuates significantly, but to a lesser degree than ion current—in a range less than one order of magnitude (Figure 3b,d). The electronic current image also changes with varying *Vs*, illustrating a nonlinear current–voltage (*I*–*V*) relation.

2.2. Transport Imaging on Polyimine/LPS Bulk Solid Electrolyte

We have previously reported that mixing polyimine particles into LPS can largely extend the cyclability of the Li/SSE/Li half-cell by effectively preventing Li dendrites, and we have proposed a model that the mechanical properties of polyimine allow the material to extend into ceramic interparticles, thus blocking dendrite growth.[29,30]

The scanning electron microscopy (SEM) and energy-dispersive X-ray spectroscopy (EDS) images show polyimine particles of ≈100-µm size and with irregular shapes (**Figure 4**), which are C- and N-rich but S- and P-poor. We took the ionic and electronic transport images on the regions of LPS, polyimine, and their boundaries. **Figure 5** shows an AFM, ionic current, and electronic current images taken on an LPS region. The ionic and electronic currents fluctuate by about one order of magnitude, and there are some topographic effects, as indicated by the ovals, which approximately agree with the previous LPS-only sample, despite the chemical weights of LPS (Li_2S 77.5: P_2S_5 22.5) differing

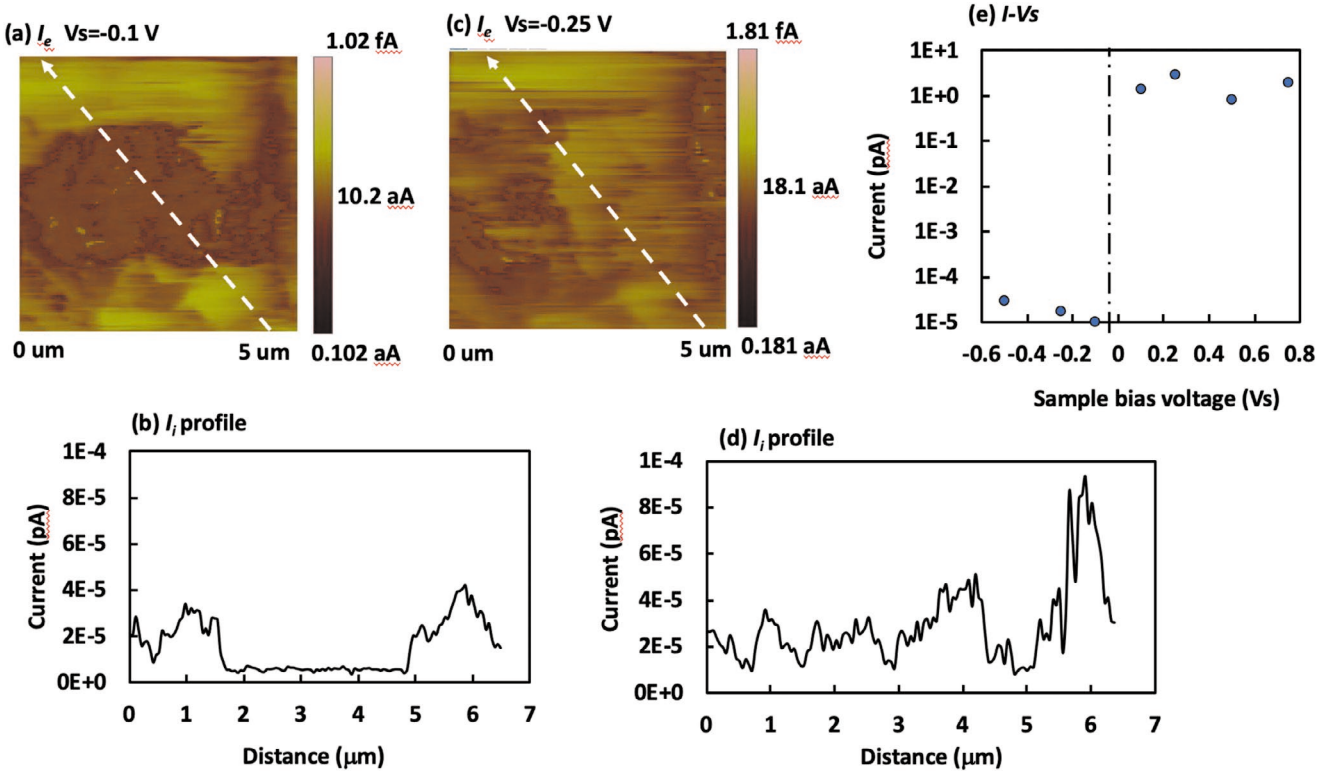

Figure 3. (a) and (c) are electronic current images taken on the same LPS area as shown in Figure 2, with negative *Vs* = –0.1 V and Vs = –0.25 V, respectively. (b) and (d) show current line profiles along the dashed lines in (a) and (c), respectively. (e) shows current–voltage data averaged from the current images.

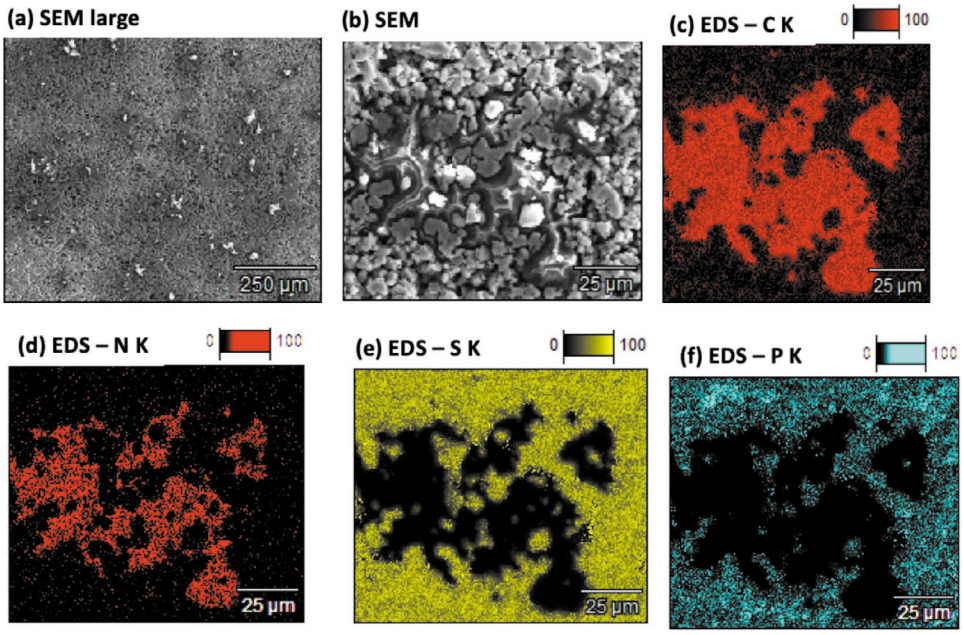

Figure 4. a) An SEM image and b–f) EDS images taken on the polyimine/LPS bulk hybrid SSE, showing the polyimine particles at sizes of ≈100 μm.

from the LPS-only sample (Li_3PS_4). The electronic current is about five orders of magnitude smaller than the ionic current (Figure 5f), which is also consistent with that of the LPS-only sample.

In the polymer region, both the ionic and electronic currents are small and below the detection limit of the amplifier, so no significant current contrast is observed (**Figure 6**a–c). We note that although the logarithm amplifier has some output

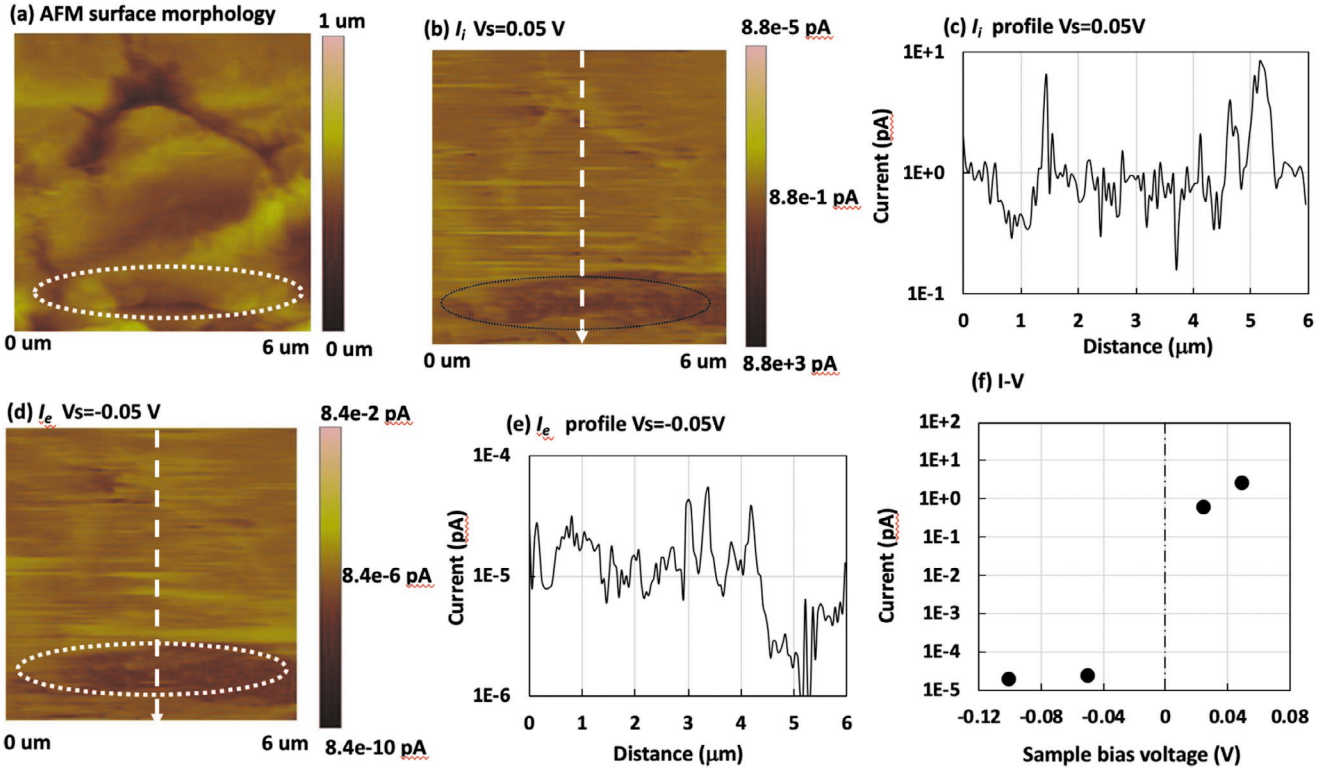

Figure 5. a) An AFM, and (b) and (d) ion and electronic current images taken on the same area of an LPS region of the polyimine/LPS hybrid SSE with bias voltages of *Vs* = +0.05 V and *Vs* = –0.05 V, respectively. (c) and (e) show current line profiles along the dashed lines in (b) and (d), respectively. (e) shows the *I–V* data averaged from the current images.

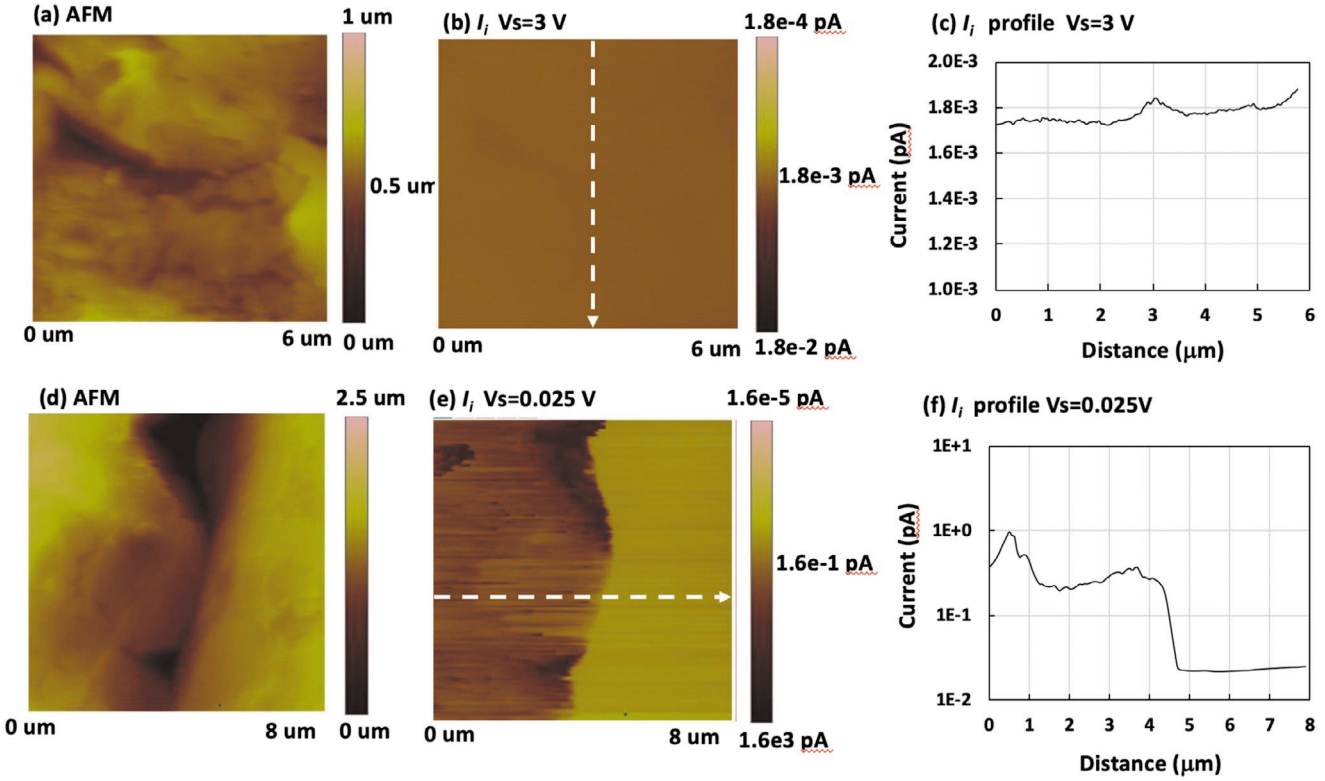

Figure 6. a) An AFM image and b) the corresponding ion current images taken on a polymer region of the polyimine/LPS hybrid SSE with large positive voltage of *V*s = +3 V. (d) and (e) show an AFM image and ion-current images on a polymer/LPS boundary. (c) and (e) show current line profiles along the dashed lines in (b) and (e), respectively.

(Figure 6c), this may not reflect the true current because the bandwidth in the small current values is very narrow. Also, the voltage applied to the sample may not be delivered to the near- surface region of the polymer particles because it is highly insulating electronically; so, the voltage drop may not be concentrated at the local nm-scale material below the probe, but rather, across the region between the probe and particle edges bordered by LPS.

By imaging the boundary region (Figure 6d–f), one sees that the ion current transition is sharp across the boundary. The current value in the near-boundary region is consistent with the regions away from the polymer particle. Therefore, the imaging results illustrate that the polymer particles have no effect on the ion current flowing through the LPS material; thus, the polymer should not be dispersed into LPS. The polymer effect of preventing Li dendrite growth is probably not caused by changing the LPS material, as was reported previously.[29,30]

In the samples mixed with the same polymer:LPS weights (30%:70%), we further found that the particle sizes in some samples are significantly smaller. **Figure 7** shows SEM-EDS images with particle sizes of ≈50 μm. Interestingly, we measured significantly smaller average ion current on the LPS region (**Figure 8**a). Similar to the model proposed previously,[29,30] the smaller polyimine particles with the same weight (polymer/LPS:30/70) should be more distributed in the LPS material bulk. Polyimine has a unique balance of elasticity and

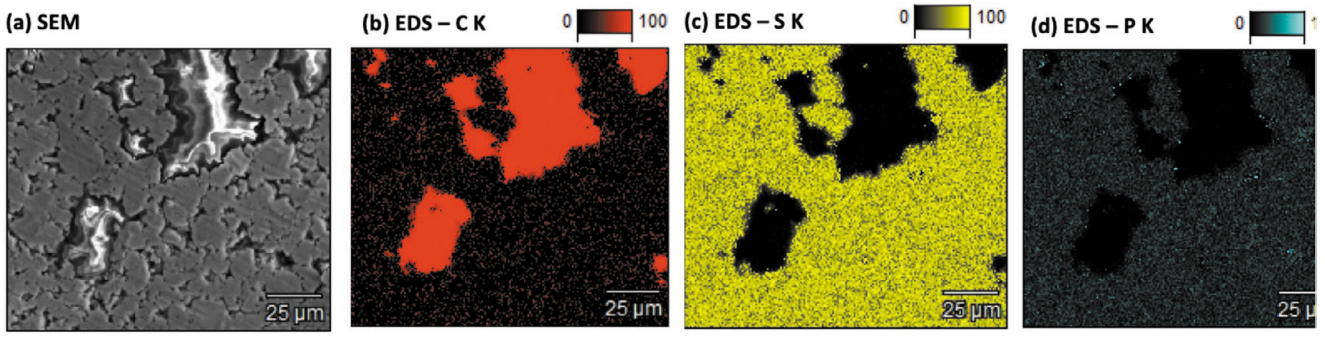

Figure 7. a) A SEM image and b–d) EDS images taken on a polyimine/LPS bulk hybrid SSE sample, showing polyimine particles at sizes of ≈50 μm, smaller than the ones shown in Figure 4.

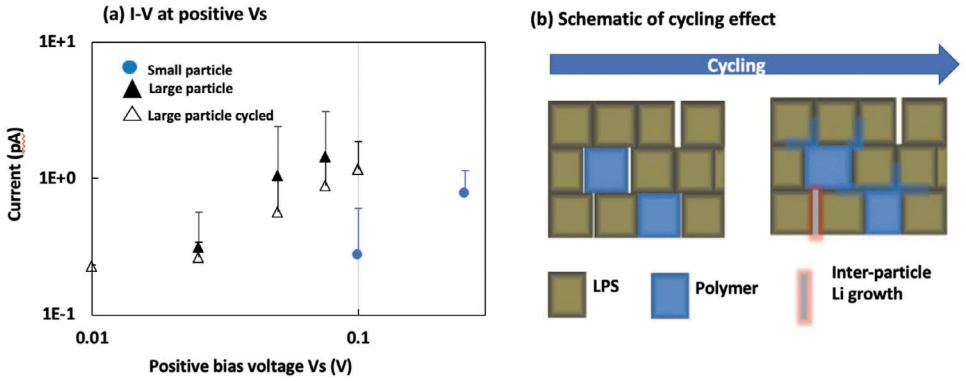

Figure 8. a) Average *I–V* data take on the polyimine/LPS hybrid SSE with small (circle symbol) and large (solid triangle) polymer particles and after the SSE was cycled (empty triangle); b) A schematic showing the model of polyimine extension into interparticles to prevent Li dendrite growth.

plasticity: it has the elasticity to block Li dendrite growth while also having the plasticity to extend into interparticles and voids. The more distributed polyimine particles probably partially blocked ion-transport routes and reduced the ion conductivity accordingly.

With galvanostatic Li plating (0.1 mA cm^{-2}), we also measured a smaller average ion current in the LPS region (Figure 8a). The extension of polyimine into interparticles by cycling effectively mitigated Li dendrite growth, as shown schematically in Figure 8b. At the same time, it also partially blocked the ion-transport routes and decreased the ion conductivity—an effect that was also shown by the galvanostatic voltage increase with cycling.[29] Therefore, mixing the polymer into LPS has two effects: it blocks both the Li dendrite growth and the ionic current flow. Optimizing the polymer weight and particle size are both necessary to improve the quality of the SSE in this approach.

3. Discussions

3.1. Ion Transport

The measured, highly nonuniform ion current can be dominated by the highly complicated ion-transport route, which depends on the local nm areas. Yang et al. proposed highly crystalline-orientation-dependent ion conduction with an activation barrier of Li+ ion "knock-off" kinetics as low as 0.08 eV, which results in the polycrystalline β-Li_3PS_4 grains behaving like a one-dimensional ion conductor along the [010] direction.[13] Another theoretical work by Klerk et al. proposed a 2D ionic conduction of the β-Li_3PS_4 within the *bc* planes.[16] Other theoretical works proposed that activation energy barriers for Li-ion interstitials and vacancy hopping are highly dependent on the crystalline orientation for both β-Li_3PS_4 and α-$Li_7P_3S_{11}$ phases.[11,12] These proposed orientation dependencies are even larger than the measured one to two orders-of-magnitude fluctuation we observed. The small LPS particle size in µm, single-crystalline domain size in hundreds of nm in the polycrystalline structure—as well as the partially disordered structure on the SSE surface and in the near-surface region—may mitigate the dependence of ion transport on grain orientations. There are no direct measurements of grain orientations or Li concentration to correlate in the imaged areas, but the particle sizes in ≈µm and single-crystalline grain sizes in hundreds of nm are approximately consistent with the overall large and small ionic current fluctuation sizes, respectively. The X-ray diffraction and SEM images of the β-Li_3PS_4 polycrystalline material are shown in Figures S1 and S2, Supporting Information. On the other hand, these structure factors can also aggravate the current fluctuation if the grain orientations among the local areas are similar or are no longer the dominant factor. To quantitatively understand the ion transport, model single-crystalline ceramics are needed with a well-ordered near-surface region and well-controlled crystalline orientations.

Also note that the hopping steps and barrier-height distribution along a conduction route associated with two specific locations will affect transport resistance. Further, the resistance may not be constant or ohmic with varying *Vs*; rather, it should depend on energy or driving voltage, as suggested by the significant change in the current image with varying *Vs*. The bias-voltage dependency of the current images varies from area to area, as we observed, and can be caused by the specific local grain orientations and local differently disordered structures. In the steady state, the ion conductance, in connection with two specific points in an ion conductor, is an integration of the conductance along all the possible hopping routes. The local current as probed by AFM is determined again by integration of all the conductance in connection with a local point in the vicinity of the probe to the probe. The inhomogeneities—such as local chemical composition, structure, ion binding energy, hopping kinetic barrier, hopping activation frequency, and hopping steps—all together determine the local ion-current fluctuation, which, as we measured, is one to two orders of magnitude in this super ion-conductor having a polycrystalline and glassy ceramic structure.

The nonuniform ion transport can be a major factor inducing Li dendrite formation and growth. In general, extended defects such as voids, crystalline defects, or disorder at the SSE/electrode interface and inside the SSE bulk are likely sources for Li dendrites.[36–39] These defects can be specific for Li ions to be reduced and trapped within; at the same time, they can also be specific for nonuniform Li-ion transport. From the perspective of thermal equilibrium, the high deviation from "equilibrium ion transport" may induce nonuniform Li accumulation and induce dendrite formation. The one to two orders-of-magnitude

fluctuation of ion-current may induce local dendrite formation from a qualitative perspective, although quantitative modeling of transport and nucleation is needed to give better understanding. A crucial question that arises from this nonuniform transport is: Even after successfully eliminating all extended structural defects, can the ion-transport fluctuations be a "secondary root cause" of Li dendrite growth? May this nonuniform transport, likely an intrinsic property of this material, solely induce formation and growth by extended charging/discharging cycling?

We also note that the nm current imaging cannot be conducted at the electrode/SSE interface by this half-cell setup. We use this setup to image the current fluctuation at the SSE side. In a real solid-state battery, the current also flows through the electrode/SSE interface and into the anode or cathode. Therefore, the current fluctuation also depends on the electrode/SSE interface. However, the current flow is already highly nonuniform at the SSE side, so it not expected to be uniform through the whole battery cell.

3.2. Electronic Transport

The small electronic current or conductance may not be adequately small for stopping Li ions to be reduced in the SSE bulk during Li-ion transport.[38] Two necessary factors for Li dendrite formation and growth should be: 1) an existing site such as a defect or a possibility to create an accommodation site for a Li atom by nonuniform ion transport; and 2) a faint electronic conductance to supply an electron to reduce the Li ion to an atom. Eliminating either one will stop the Li dendrite formation from the SSE bulk. The five orders-of-magnitude smaller electronic current is obviously not adequate, considering that the amount of Li atoms in a dendrite must be much more than orders-of-magnitude less than in the Li plating before a dendrite can grow enough to short a device. Therefore, increasing the electronic resistivity of SSE is another approach to prevent dendrite formation inside the SSE bulk.

The ionic ceramic material is essentially an electronic insulator, with all the valence electronic state localized around the atom cores and all the valence states filled. However, small defects—even such as a point defect of a single atomic vacancy or interstitial—can create an unoccupied valence hole or occupied anti-bonding electrons. These densities of states are highly localized, so they do not create dispersed bands, and they essentially make the materials electronically insulating. However, overlap of the electronic states or wavefunction still exists, although it is much less than most of the semiconductors that have unavoidable defect doping. Electrons or holes can hop across the states by the overlap and form electrical conduction percolations. Therefore, passivation of defects can be an approach to prevent Li dendrite growth from the perspective of blocking electronic conduction.

4. Conclusions

Nm-scale ionic and electronic transport in the LPS and polymer/ceramic hybrid SSE was imaged by using a logarithm amplifier. The results show one to two orders-of-magnitude nonuniform local ion conductivity, which to our knowledge is new information to the SSB community. We discussed the results from the perspective of intrinsic anisotropic kinetic barriers along the different crystalline axes, which suggests necessary mitigation—maybe second to the extended defect and SSE/electrode interface origins—to prevent Li dendrite formation and growth. The results on the bulk hybrid SSE show a sharp transition of ion transport at the boundary of polyimine/LPS and decreases of the ion current with smaller polyimine particles and with cycling, which corroborate the mechanism of polyimine extension into interparticles to block Li dendrite growth. From these results, we further propose the need to optimize polymer weight and particle size to balance the ion conductivity and cyclability of the SSE. This work opens up novel characterization of ionic and electronic transport, which relates directly to plating and stripping of Li for SSBs. Expanding the ionic and electronic transport imaging to composite materials such as involving binders and involving different crystallinities, textures, and grain orientations is expected to further impact the development of SSBs.

5. Experimental Section

Ionic and Electronic Imaging: A logarithm-scale current amplifier was used to enhance the current sensitivity to a wide range of mA to fA. However, the bandwidth of the amplifier was narrow and depended on sample materials and probe configurations. So, the accuracy of the amplifier output with a small current around the fA range was low, and response time of the amplifier to a current change was slow. Furthermore, these parameters were impossible to quantify at that time without a proper standard sample in the highly resistive ranges. However, the qualitative relative output was reliable, for example, in the same image, the qualitative comparison of higher and lower current was reliable. Therefore, the measured electronic leaking current fluctuation was rather qualitative. The AFM (Veeco D5000 and Nanoscope V) was set up in an Ar glove box to avoid oxidation of the SSE. To take one image, the scanning time with *Vs* applied to the sample typically took 10–30 min, depending on the scan rate and scanning lines. The overall current fluctuation and AFM topography did not change during the scanning, and the parameters of scanning time and rate were determined by the image quality. Each current data in a *I*–*V* relation were averaged from an image with 512 × 256 or 512 × 128 resistance pixels. The data on the same type of sample were averaged from multiple images to get the averaged current and standard deviation. For example, Figure 8 was obtained by 53 resistance images. The current was converted from the measured resistance by $I = Vs/R$, where *Vs* and *R* were, respectively, applied bias voltage to the sample and measured resistance.

The voltage applied was to keep the ion current below ≈10 pA. If the current was larger than that, the local current density was too high and sample damage might occur. The applied voltage was adjusted to keep the ion current less than on the order of ≈10 pA. For example, the different *Vs* applied between the LPS and hybrid SSE was because of their conductivity difference. The large *Vs* (3V) applied in the polymer region of hybrid SSE was because the region was insulating, with no detectable current flows in this region even under a large *Vs* of 3 V. In the LPS and mixed regions, a much smaller *Vs* was applied to keep the current from overflowing.

Diamond-coated Si probes with a probe curvature radius of ≈100 nm (BrukerNano DDESP-V2) were used to enhance the probe wear-off. However, the probe/sample contact size was unknown and had to be smaller than the probe diameter of 200 nm—perhaps roughly in the

range of 10–200 nm (Figure 1c). The current density was 1 mA cm^{-2} to 10 μA cm^{-2} at the detection limit with a contact size of 10–200 nm, which was comparable to a normal battery charging/discharging current density. Therefore, the current detection limit in fA was applicable for the transport imaging on the SSE. The current route spread rapidly with distance away from the probe, so the voltage drop concentrated on the area directly beneath the probe. In other words, the measured resistance was primarily dominated by that of the local area beneath the probe, so the imaging had nm-scale resolution.[41,42]

SSE Preparations: The β-Li_3PS_4 (LPS) powder was synthesized in a glove box with Ar atmosphere (with the O_2 and H_2O content both under 5 ppm) via a solution method. High-purity precursors of Li_2S (99.98%) (Aldrich) and P_2S_5 (99%) (Aldrich) were used as-received, and anhydrous THF solvent (99.9%) (Aldrich) was pretreated with molecular sieves to remove residual water before use. Li_2S (0.244 g) and P_2S_5 (0.394 g) powders were mixed in the dried-THF solution under stirring for 24 h. The above solution was then dropped onto a Kevlar mat, followed by overnight pre-drying in an antechamber under evacuation condition, forming an LPS@Kevlar membrane. The as-prepared LPS@Kevlar membrane was dried in a furnace in the glove box for 24 h at 140 °C and then further dried in a vacuum oven for 24 h at 140 °C. To obtain a dense electrolyte, all the membranes were pressed under 500 Mpa pressure before use.

The polyimine/LPS hybrid SSE was made by gently mixing polyimine and LPS powders (3:7 – polyimine:LPS) with mortar and pestle. 100 mg of the polymer/LPS composite was then collected and cold compacted (5 ton force) into a free-standing pellet with an hydraulic hand press.

Scanning Electron Microscopy Observation: SEM imaging and EDS analysis was performed in an FEI Nova Nanolab 200 dual-beam focused ion beam (FIB) workstation using a Thermo Fisher Pathfinder windowless EDS system. An electron-beam accelerating voltage of 5 kV was used for the EDS analysis.

Supporting Information

Supporting Information is available from the Wiley Online Library or from the author.

Acknowledgements

C.J., H.G., and M.A. acknowledge funding support by the Laboratory Directed Research and Development (LDRD) program at NREL. S.-H.L. acknowledges financial support from a National Research Foundation of Korea grant (NRF-2018M1A2A2063340). Y.L. and P.L. acknowledge funding support by the Advanced Research Projects Agency–Energy, U.S. Department of Energy, under Contract No. DE-AR0000781.

Conflict of Interest

The authors declare no conflict of interest.

Keywords

atomic force microscopy, ion transport, Li_3PS_4, nanometer resolution, polymer/ceramic hybrid, solid-state electrolyte

Received: January 19, 2020
Revised: March 16, 2020
Published online:

[1] P. H. L. Notten, F. Roozeboom, R. a. H. Niessen, L. Baggetto, *Adv. Mater.* **2007**, *19*, 4564.
[2] J. Trevey, J. S. Jang, Y. S. Jung, C. R. Stoldt, S.-H. Lee, *Electrochem. Commun.* **2009**, *11*, 1830.
[3] K. Fu, Y. Gong, B. Liu, Y. Zhu, S. Xu, Y. Yao, W. Luo, C. Wang, S. D. Lacey, J. Dai, Y. Chen, Y. Mo, E. Wachsman, L. Hu, *Sci. Adv.* **2017**, *3*, e1601659.
[4] W. Luo, Y. Gong, Y. Zhu, Y. Li, Y. Yao, Y. Zhang, K. (Kelvin) Fu, G. Pastel, C.-F. Lin, Y. Mo, E. D. Wachsman, L. Hu, *Adv. Mater.* **2017**, *29*, 1606042.
[5] P. Knauth, *Solid State Ion.* **2009**, *180*, 911.
[6] V. Thangadurai, S. Narayanan, D. Pinzaru, *Chem. Soc. Rev.* **2014**, *43*, 4714.
[7] J. C. Bachman, S. Muy, A. Grimaud, H.-H. Chang, N. Pour, S. F. Lux, O. Paschos, F. Maglia, S. Lupart, P. Lamp, L. Giordano, Y. Shao-Horn, *Chem. Rev.* **2016**, *116*, 140.
[8] P. Bron, B. Roling, S. Dehnen, *J. Power Sources* **2017**, *352*, 127.
[9] H. Stöffler, T. Zinkevich, M. Yavuz, A.-L. Hansen, M. Knapp, J. Bednarčík, S. Randau, F. H. Richter, J. Janek, H. Ehrenberg, S. Indris, *J. Phys. Chem. C* **2019**, *123*, 10280.
[10] T. M. Arruda, A. Kumar, S. V. Kalinin, S. Jesse, *Nano Lett.* **2011**, *11*, 4161.
[11] N. D. Lepley, N. a. W. Holzwarth, *J. Electrochem. Soc.* **2012**, *159*, A538.
[12] N. D. Lepley, N. A. W. Holzwarth, Y. A. Du, *Phys. Rev. B* **2013**, *88*, 104103.
[13] Y. Yang, Q. Wu, Y. Cui, Y. Chen, S. Shi, R.-Z. Wang, H. Yan, *ACS Appl. Mater. Interfaces* **2016**, *8*, 25229.
[14] M. Xu, J. Ding, E. Ma, *Appl. Phys. Lett.* **2012**, *101*, 031901.
[15] Y. Mo, S. P. Ong, G. Ceder, *Chem. Mater.* **2012**, *24*, 15.
[16] N. J. J. de Klerk, E. van der Maas, M. Wagemaker, *ACS Appl. Energy Mater.* **2018**, *1*, 3230.
[17] H. Yamane, M. Shibata, Y. Shimane, T. Junke, Y. Seino, S. Adams, K. Minami, A. Hayashi, M. Tatsumisago, *Solid State Ion.* **2007**, *178*, 1163.
[18] H. Muramatsu, A. Hayashi, T. Ohtomo, S. Hama, M. Tatsumisago, *Solid State Ion.* **2011**, *182*, 116.
[19] N.-W. Li, Y.-X. Yin, C.-P. Yang, Y.-G. Guo, *Adv. Mater.* **2016**, *28*, 1853.
[20] N. Ohta, K. Takada, I. Sakaguchi, L. Zhang, R. Ma, K. Fukuda, M. Osada, T. Sasaki, *Electrochem. Commun.* **2007**, *9*, 1486.
[21] J. Haruyama, K. Sodeyama, L. Han, K. Takada, Y. Tateyama, *Chem. Mater.* **2014**, *26*, 4248.
[22] M. Fingerle, R. Buchheit, S. Sicolo, K. Albe, R. Hausbrand, *Chem. Mater.* **2017**, *29*, 7675.
[23] S. Wenzel, D. A. Weber, T. Leichtweiss, M. R. Busche, J. Sann, J. Janek, *Solid State Ion.* **2016**, *286*, 24.
[24] J. Lau, R. H. DeBlock, D. M. Butts, D. S. Ashby, C. S. Choi, B. S. Dunn, *Adv. Energy Mater.* **2018**, *8*, 1800933.
[25] T. Swamy, X. Chen, Y.-M. Chiang, *Chem. Mater.* **2019**, *31*, 707.
[26] Y. Zhu, X. He, Y. Mo, *ACS Appl. Mater. Interfaces* **2015**, *7*, 23685.
[27] R. Garcia-Mendez, F. Mizuno, R. Zhang, T. S. Arthur, J. Sakamoto, *Electrochim. Acta* **2017**, *237*, 144.
[28] J. W. Fergus, *J. Power Sources* **2010**, *195*, 4554.
[29] J. M. Whiteley, S. Hafner, C. Zhu, W. Zhang, S.-H. Lee, *J. Electrochem. Soc.* **2017**, *164*, A2962.
[30] J. M. Whiteley, P. Taynton, W. Zhang, S.-H. Lee, *Adv. Mater.* **2015**, *27*, 6922.
[31] S. H. Chung, Y. Wang, L. Persi, F. Croce, S. G. Greenbaum, B. Scrosati, E. Plichta, *J. Power Sources* **2001**, *97–98*, 644.
[32] K. Nairn, M. Forsyth, H. Every, M. Greville, D. R. MacFarlane, *Solid State Ion.* **1996**, *86–88*, 589.
[33] F. Langer, I. Bardenhagen, J. Glenneberg, R. Kun, *Solid State Ion.* **2016**, *291*, 8.
[34] I. Yoshimatsu, T. Hirai, J. Yamaki, *J. Electrochem. Soc.* **1988**, *135*, 2422.
[35] C. Monroe, J. Newman, *J. Electrochem. Soc.* **2005**, *152*, A396.

[36] L. Porz, T. Swamy, B. W. Sheldon, D. Rettenwander, T. Frömling, H. L. Thaman, S. Berendts, R. Uecker, W. C. Carter, Y.-M. Chiang, *Adv. Energy Mater.* **2017**, *7*, 1701003.
[37] K. J. Harry, D. T. Hallinan, D. Y. Parkinson, A. A. MacDowell, N. P. Balsara, *Nat. Mater.* **2014**, *13*, 69.
[38] F. Han, A. S. Westover, J. Yue, X. Fan, F. Wang, M. Chi, D. N. Leonard, N. J. Dudney, H. Wang, C. Wang, *Nat. Energy* **2019**, *4*, 187.
[39] F. Shen, M. B. Dixit, X. Xiao, K. B. Hatzell, *ACS Energy Lett.* **2018**, *3*, 1056.
[40] L. Pan, L. Zhang, A. Ye, S. Chi, Z. Zou, B. He, L. Chen, Q. Zhao, D. Wang, S. Shi, *J. Materiomics* **2019**, *5*, 688.
[41] P. Eyben, F. Clemente, K. Vanstreels, G. Pourtois, T. Clarysse, E. Duriau, T. Hantschel, K. Sankaran, J. Mody, W. Vandervorst, K. Mylvaganam, L. Zhang, *J. Vac. Sci. Technol. B* **2010**, *28*, 401.
[42] L. Zhang, K. Ohuchi, K. Adachi, K. Ishimaru, M. Takayanagi, A. Nishiyama, *Appl. Phys. Lett.* **2007**, *90*, 192103.
[43] C. Stetson, T. Yoon, J. Coyle, W. Nemeth, M. Young, A. Norman, S. Pylypenko, C. Ban, C.-S. Jiang, M. Al-Jassim, A. Burrell, *Nano Energy* **2019**, *55*, 477.